PAPER

A comparative study of electrical and opto-electrical properties of a few-layer p-WSe₂/n-WS₂ heterojunction diode on SiO₂ and h-BN substrates†

Pradeep Raj Sharma,[a] Praveen Gautam,[a] Amir Muhammad Afzal,[b]
Byoungchoo Park [ID][b] and Hwayong Noh [ID]*[a]

Since the innovation of van der Waals heterostructures of 2D materials, the p–n junction diode, a building block of electronics and opto-electronics has been studied in various ways. To date most of them have been studied on SiO₂ or other oxide substrates, although the oxide substrates cause significant degradation of the 2D material's intrinsic properties and device performances. Whereas using hexagonal boron nitride (h-BN) as an underlying layer to the 2D materials is known to preserve their properties. Here we have carefully analyzed the electrical and opto-electrical properties of a p-WSe₂/n-WS₂ van der Waals heterojunction diode on SiO₂ and the h-BN substrates. Besides the usual enhancement of the field-effect mobility of WSe₂ and WS₂, we have achieved a significant enhancement of the diode rectification ratio and excellent photovoltaic characteristics on the h-BN substrate. We have obtained more than an order-of-magnitude enhancement of the diode rectification ratio and about two-fold increments in the overall opto-electronics behavior on the h-BN substrate compared with those on the SiO₂ substrate. The values of self-powered photo responsivity and external quantum efficiency are 3 A/W and 588% respectively on the h-BN substrate at 10 mW cm⁻² photo-power density and 633 nm wavelength, whereas they reduce to about one-half on the SiO₂ substrate.

Introduction

Graphene has been excessively studied in the field of electronics,[1,2] optoelectronics[3,4] and spintronics,[5–7] although the zero band-gap nature of pristine graphene hinders its application in electronic devices.[8,9] On the other hand, the 2D transition metal dichalcogenide (TMD) materials with a band-gap ranging from 1 eV to 2 eV depending on their layer thickness are excellent alternatives to graphene.[10] The band-gap also varies from a multilayer indirect gap to a monolayer direct gap,[11,12] providing possibilities for wide application such as in photo-detectors,[13,14] optical communication,[15,16] and field-effect transistors.[17,18] Among the TMD family, tungsten (W) and molybdenum (M) based TMDs are in great demand due to their unique and superior semiconducting and optoelectronic properties.[19–21] Of the W-based TMDs, tungsten disulphide (WS₂) has attracted much attention because of its high field-effect mobility, larger spin–orbit coupling,[22,23] high photo sensitivity in the visible region,[24] and abundance in n-type doping.

Similarly tungsten diselenide (WSe₂) is at the apex of interest because of its high mobility, less degradation in an ambient environment,[25] high photo-absorbance coefficient in the longer wavelength region, and dominant p-type doping.[26–28] Formation of a p–n heterojunction between p-WSe₂ and n-WS₂ produces a strong type-II band alignment and hence a high built-in potential,[29,30] which is excellent for opto-electronic device applications. Among the different types of van der Waals (vdW) p–n heterojunction diodes, the lateral–vertical heterostructure has attracted considerable attention and showed better performance, whereas few studies have been done on a true vertical or in-plane lateral heterojunction structure.[31–33]

Since the beginning, almost all the research work on the vdW p–n heterojunction diode has been done on SiO₂ or other oxide substrates.[34] Experimental findings suggest that the qualities of 2D materials including graphene, TMDs, and many others on the oxide substrate were affected by various factors such as scattering from charged surface states, surface impurities, and surface roughness.[35–37] In particular, the charge impurities trapped at the interface between the 2D material and SiO₂ were found to change the intrinsic properties of the materials.[38] Furthermore, it has been proved that the major source of hysteresis, which hinders the device performance and stability, also arises from the trapped charges. Without addressing these problems, we cannot obtain a fine tune of the material's intrinsic characteristics and realize the actual device

[a]Department of Physics and Astronomy, Sejong University, Seoul 05006, Republic of Korea. E-mail: hnoh@sejong.ac.kr

[b]Department of Electrical and Biological Physics, Kwangwoon University, Seoul 01897, Republic of Korea

performance and stability, which was overlooked by most of the research done before on the p–n junction diodes.[29–33] Among the 2D materials, hexagonal boron nitride (h-BN) is known to be a good supporting substrate to address those problems, owing to the inert nature, high band-gap energy (5.5 eV), and high dielectric constant (~4).[35] Furthermore, atomically planner and smooth surface of h-BN reduces the rippling in the 2D materials, lowers the trapped charge density, and also reduces the hysteresis, thereby enhancing the field-effect mobility of the 2D materials.[36,38–40]

Herein we report a comparative study of electronic and optoelectronic behaviors of p-WSe$_2$/n-WS$_2$ heterojunction diodes fabricated on both SiO$_2$ and h-BN substrates. Our main motivation towards this work is to systematically study the substrate's influence on the device performances. We observed more than an order-of-magnitude increment of the diode rectification ratio on the h-BN substrate than on the SiO$_2$ substrate. Moreover, the calculated photovoltaic parameters indicate significantly improved photo-electric behaviors in h-BN supported device as compared to SiO$_2$ supported device.

Experimental

Device fabrication

A mechanical exfoliation technique with a transparent polydimethylsiloxane (PDMS) stamp was used to transfer suitable TMD and h-BN flakes from high quality natural bulk crystals. The WS$_2$ crystal was purchased from 2D semiconductors, and WSe$_2$ and h-BN crystals from HQ graphene. Flakes of each material were mechanically exfoliated by using an adhesive tape. Then, they were picked up by a PDMS stamp on a glass slide for the transfer process. The uniformity and the thickness of the exfoliated flakes were roughly identified with an optical microscope before the transfer, and confirmed later by the atomic force microscopy (AFM). Placing the PDMS stamp on a target substrate and peeling it off transfers the flakes to the substrate. Successive transfers of few layers (FL) WSe$_2$ and FL WS$_2$ on the SiO$_2$/Si substrate makes a WS$_2$/WSe$_2$/SiO$_2$ lateral–vertical p–n vdW heterojunction diode, now onward named as device1. To prepare the h-BN substrate, a large uniform multilayer h-BN flake was first transferred onto another SiO$_2$/Si substrate and then it was annealed at 300 °C for 2 hours in high vacuum (>10^{-6} torr) to remove the residues present. Finally, FL WSe$_2$ and FL WS$_2$ flakes were successively transferred over the h-BN so that it makes a WS$_2$/WSe$_2$/h-BN/SiO$_2$ lateral–vertical p–n heterojunction diode, now onward named as device2. The transfer of each flake was precisely controlled with a microaligner stage monitored by a CCD camera. After the transfer of each TMD flake it was passed through a 1 hour hot acetone bath to remove the PDMS and tape residues. For the electrodes, a high work-function metal Pd for the p-type WSe$_2$ and a low work-function metal Al for the n-type WS$_2$ were deposited followed by a 60 nm-thick Au cap layer under high vacuum condition. Optical microscope images of the device1 and device2 are shown in Fig. 1(a) and (b), respectively, and their schematics in (c) and (d), respectively. With the two contacts

placed on each of the TMD flakes, electrical characteristics of each TMD or the heterojunction could be measured.

Measurements

Raman spectroscopy for the devices were done with Renishaw RE04 model with the wavelength of 514 nm under 1 mW power and laser spot size of about 1 μm. Height profiles of the devices were measured with an AFM (NanoFocus) along with the surface topography. For electrical transport measurements we have used Keithley 2400 source-meter and Keithley 6485 pico-ammeter. Photoresponse was measured using a wave generated by LGK 7654-13 He–Ne laser (633 nm) under vacuum condition.

Results and discussion

Raman spectroscopy and AFM

The Raman spectroscopy data for both devices at the heterojunction region are shown in Fig. 1(e) and (f). The two typical Raman active modes of WSe$_2$, E$_{2g}^1$ (250 cm^{-1}) and A$_{1g}$ (260 cm^{-1}), were observed.[41] Similarly we obtained two Raman peaks at 350 and 420 cm^{-1}, representing E$_{2g}^1$ and A$_{1g}$ modes of WS$_2$.[42] Raman peaks from the substrates, Si (520 cm^{-1}) for the device1 and both Si (520 cm^{-1}) and h-BN (1350 cm^{-1}) for the device2 are also shown. Detailed spectrums of each individual flake of WS$_2$ and WSe$_2$ are shown in Fig. S1.† Furthermore, we conducted an AFM (NanoFocus) measurement to verify the flake thicknesses. Fig. S2(a) and (b)† show the combined height profile of WSe$_2$ (~5.8 nm) and WS$_2$ (~8.0 nm) of device1 and WSe$_2$ (~5.6 nm) and WS2 (~8.8 nm) of device2 with inset AFM topographic images. The thickness of h-BN is 30 nm as shown in Fig. S2(c).†

Electrical characteristics of p-WSe$_2$/n-WS$_2$ heterojunction

The transfer characteristics curve, source-drain current (I_{ds}) as a function of back-gate voltage (V_{bg}), of WSe$_2$ on the two devices at a source-drain voltage (V_{ds}) of 1 V are plotted in Fig. 2(a) and (b). The increment of I_{ds} at negative V_{bg} confirms the p-type nature of WSe$_2$ on both substrates. Fig. 2(c) and (d) show the transfer characteristics curve of WS$_2$ on both devices, where the n-type nature of WS$_2$ is confirmed from the increment of I_{ds} at positive V_{bg}. The field-effect mobility (μ_{FE}) and the I_{ON}/I_{OFF} ratio of each TMD were calculated in both devices to analyze the electrical performance. We have used the relation below to extract μ_{FE} of the TMDs in both devices.

$$\mu_{FE} = \frac{L}{W C_{bg} V_{ds}} \left(\frac{dI_{ds}}{dV_{bg}} \right) \tag{1}$$

where L and W denote the length and width of the TMDs channel, $\left(\frac{dI_{ds}}{dV_{bg}} \right)$ is the slope of the linear part of transfer characteristics curve, and C_{bg} is the gate-capacitance of the substrates. The gate-capacitance can be calculated by $C_{bg} = \frac{\varepsilon_r \varepsilon_0}{d}$[43,44] where ε_r is the relative permittivity of SiO$_2$ (3.9) and d is the thickness. The value of C_{bg} we have obtained is
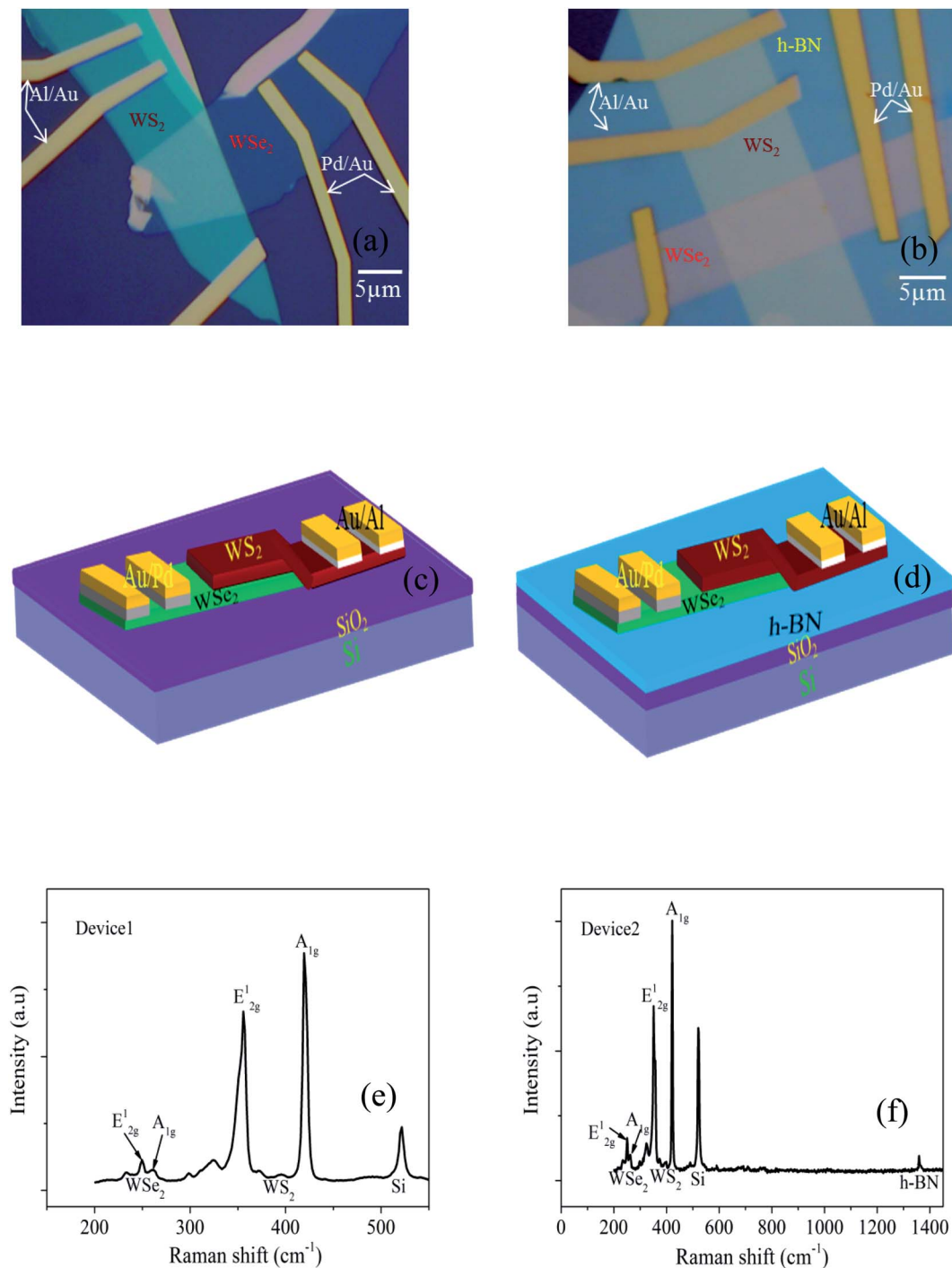
Fig. 1 (a) and (b) An optical microscopic image of the p-WSe$_2$/n-WS$_2$ heterojunction diode of device1 and device2 respectively. (c) and (d) Schematic device geometry of device1 and device2, respectively. (e) and (f) Raman spectra of device1 and device2 at the junction with laser excitation wavelength of 514 nm.

287 μF m^{-2}. For the h-BN/SiO$_2$ structure, the gate-capacitance should include the contribution of both dielectrics being that of two capacitors in series but the h-BN could be neglected since its thickness is much smaller than the SiO$_2$. The mobility of WS$_2$ and WSe$_2$ we obtained in device2 was 100 and 40 cm^2 V^{-1} s^{-1} respectively, which is about 2 times higher than those measured in device1. The I_{ON}/I_{OFF} ratio in device 2 increases about an

order-of-magnitude reaching 10^5 for WSe$_2$ and a three-fold increment for WS$_2$ as compared to those in device1. The main reason behind the significant enhancement in the filed-effect mobility and I_{ON}/I_{Off} ratio of the TMDs in device2 is the use of the h-BN substrate, as explained by the articles published.[35,43,45] Furthermore, the charge injection from suitable metal contacts into the TMDs also helps to enhance the device characteristics
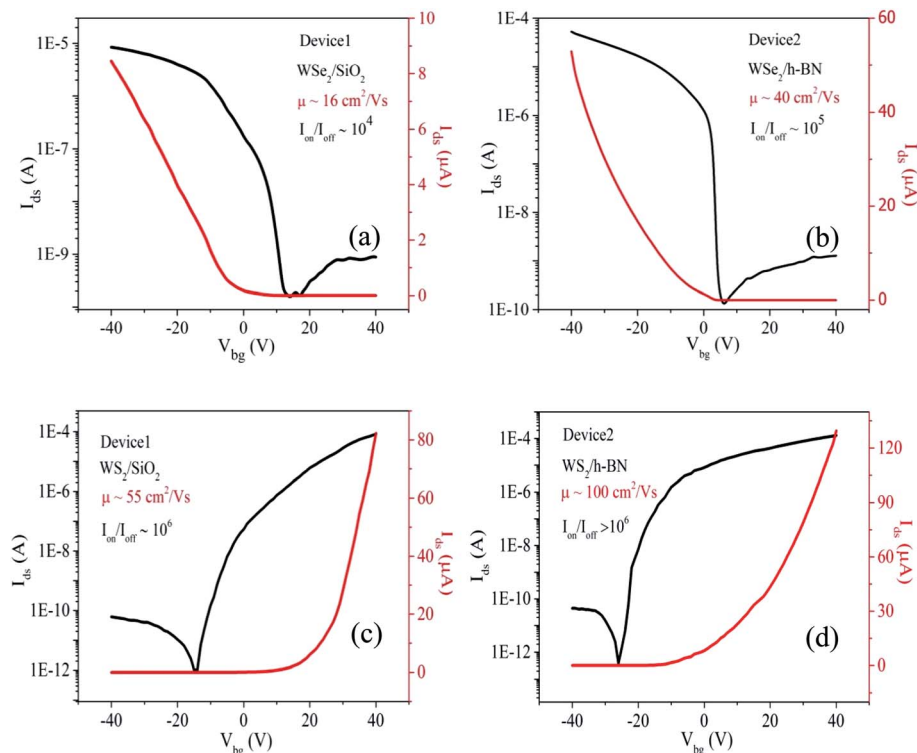
Fig. 2 Transfer characteristics curve (I_{ds}–V_{bg}) of each FL flake on different substrates at $V_{ds} = 1$ V. (a) and (b) FL-WSe$_2$ showing p-type characteristic on SiO$_2$ and h-BN substrates respectively. (c) and (d) FL-WS$_2$ showing n-type characteristic on SiO$_2$ and h-BN substrate respectively.
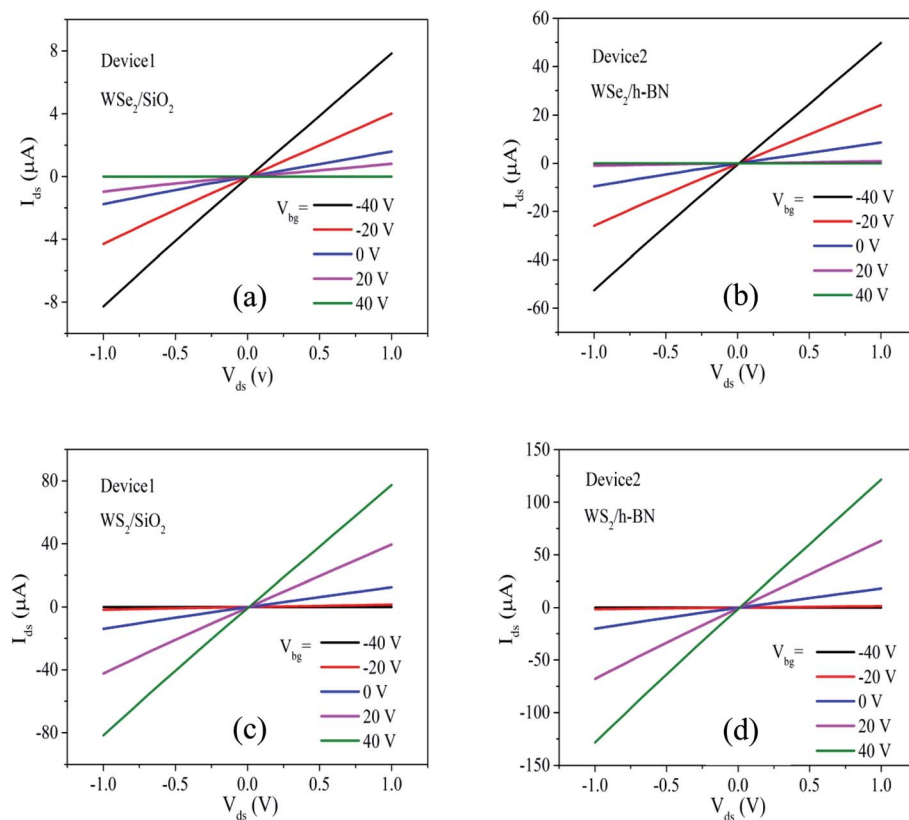

Fig. 3 Linear I_{ds}–V_{ds} characteristics curve of TMDs at different V_{bg} on different substrates. (a) and (b) FL-WSe$_2$ on SiO$_2$ and h-BN substrates respectively. (c) and (d) FL-WS$_2$ on SiO$_2$ and h-BN substrates respectively.
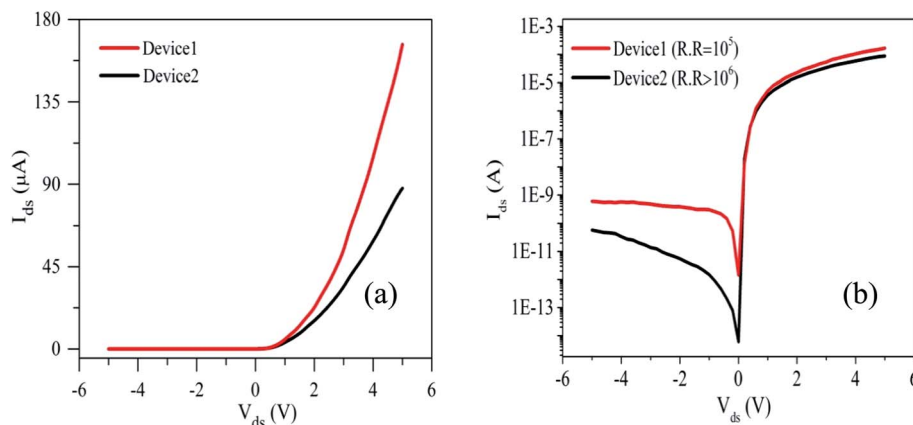
Fig. 4 Diode (I_{ds}–V_{ds}) characteristics curves of p-WSe$_2$/n-WS$_2$ heterojunction at $V_{bg} = -40$ V. (a) Linear scale (b) semi-log scale.

as suggested by articles.[46,47] Pd is one of the best contact metal for an efficient hole injection into WSe$_2$ because of its high work-function and better alignment to the valance band of WSe$_2$,[27,48] whereas low work-function metal Al is one of the suitable candidates for n-type materials and hence reduces the Schottky barrier height (SBH), thereby making ohmic contacts. Fig. 3(a) and (b) illustrate the current–voltage (I_{ds}–V_{ds}) curves of p-WSe$_2$ on device1 and device2, respectively, whereas (c) and (d) show those of n-WS$_2$ on device1 and device2, respectively, at different back-gate voltages. The contacts between the metal and the TMD in both devices show linear behavior, insuring low contact resistance.

Now we discuss the rectification behavior of the p-WSe$_2$/n-WS$_2$ heterojunction diode. The I_{ds}–V_{ds} characteristics curves of the p–n heterojunction with $V_{bg} = -40$ V is shown in Fig. 4. Diode rectification ratio (RR) was defined by the ratio of the forward current (I_f) to the reverse current (I_r), RR $= \dfrac{I_f}{I_r}$. We have observed the diode RR as high as 10^5 in device1, which is in the range of previously reported values on the SiO$_2$ substrate,[49,50] whereas an order-of-magnitude enhancement is achieved in device2 (h-BN substrate) with RR > 10^6. There are several different factors influencing the diode RR. The diode RR was believed to be limited by a high SBH of the metal/TMD interface. This limiting effect was confirmed after the achievement of a high diode RR with an ohmic metal/TMD interface and a much reduced SBH.[51] As another factor, the sharpness of the interface between the TMDs at the junction is still under debate.[32,52] Generally most of the diode characteristics have been studied in a lateral–vertical vdW heterojunction structure, where lateral channels are also present in addition to the heterojunction.[32,53] The diode RR in a true vertical heterojunction without the lateral channel was found significantly lower than the lateral–vertical heterojunction.[32] It suggests that the planer TMD channel along with the vertical TMD junction plays a crucial role. Most of all, the h-BN substrate plays an important role to enhance the diode RR in our experiment as compared with the SiO$_2$ substrate. If we compare the semi-log plot of the I_{ds}–V_{ds} curves at $V_{bg} = -40$ V in Fig. 4(b), the reverse current in device2 (h-BN substrate) is about an order-of-magnitude

smaller whereas the forward current is slightly lower than those of device1 (SiO$_2$ substrate). This suggests that the TMD/SiO$_2$ interface introduces more trap states, which cause the large reverse current as well as the unintentional forward current.[54] The reduction of hysteresis behavior in device2 as compared to device1 further confirms less trapped states at the TMD/h-BN interface, as shown in Fig. S3.† Furthermore, the h-BN substrate significantly reduces the surface defects and provides a flat and inert base for the device. Therefore, our p–n heterojunction diode in device2 showed much improved I_{ds}–V_{ds} characteristics as compared to device1. We also show the V_{bg} dependent I_{ds}–V_{ds} characteristics curves in Fig. S4.†

Opto-electrical characteristics of p-WSe$_2$/n-WS$_2$ heterojunction

Along with the excellent electric properties, the p-WSe$_2$/n-WS$_2$ lateral–vertical heterojunction also exhibits superior photovoltaic properties. The output (I_{ds}–V_{ds}) curves under different photo-power densities (P) of 10, 30, 50, and 70 mW cm^{-2} at the wavelength (λ) of 633 nm are shown in Fig. 5(a) and (b) for device1 and device2. In both devices we observed a significant change in the I_{ds}–V_{ds} characteristics with photo powers. Huo *et al.*[30] also observed a large photo response in a p-WSe$_2$/n-WS$_2$ heterojunction that is comparable to our results in device1. The large photovoltaic behavior occurs mainly due to the type-II band alignment and the high built-in potential at the heterointerface, which can effectively separate the photo-excited electron–hole pairs. These electrons and holes are accumulated towards the n-WS$_2$ and p-WSe$_2$, respectively, and lead to the formation of an open-circuit voltage (V_{OC}), the P-dependence of which is shown in Fig. 5(c). These accumulated electrons and holes in WS$_2$ and WSe$_2$ recombine rapidly through an external circuit leading to the generation of a short-circuit current (I_{SC}) at zero V_{ds}, as shown in Fig. 5(d). We observed larger values of V_{OC} and I_{SC} in device2 than in device1, which is attributed to the excellent photo absorption and efficient photo-induced electron–hole pair generation in device2 as compared to that of device1. Accordingly, a significantly improved time dependent photocurrent is observed in device2 compared to
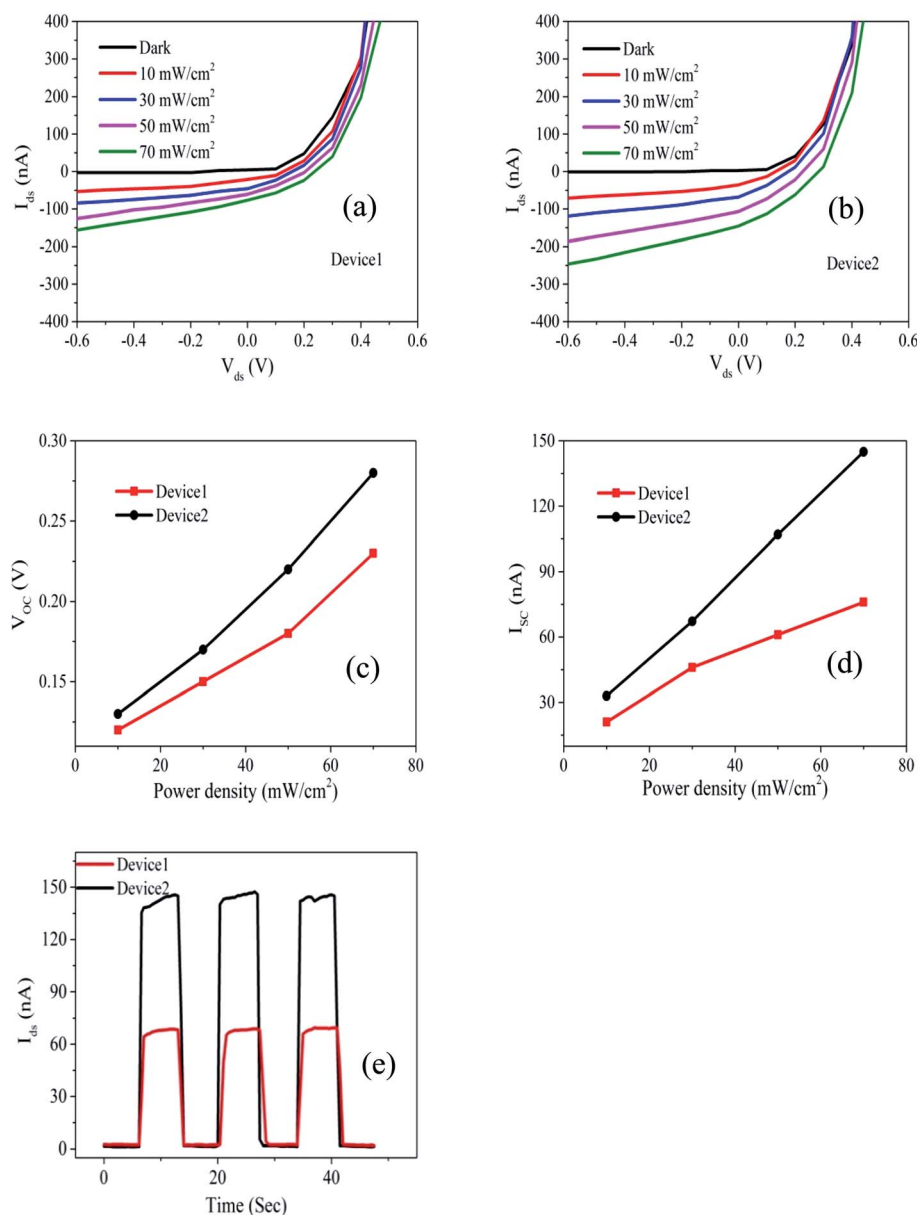
Fig. 5 Photo responses of p-WSe$_2$/n-WS$_2$ heterojunction on different substrates under the illumination of light wavelength of 633 nm (at 0 V$_{bg}$). (a) and (b) I_{ds}–V_{ds} characteristics curves under different power density on SiO$_2$ and h-BN substrates respectively. (c) V_{OC} (d) I_{SC} plotted as a function of power density. (e) The dynamic response of both devices with P = 70 mW cm^{-2} at 0 V$_{ds}$ and 0 V$_{bg}$.

that of device1 as shown in Fig. 5(e). The photocurrent can be instantly generated and declined with switching the light on and off. Basically, the h-BN substrate makes an inert and flat surface, which reduces the scattering effects and the trap states.[49,50] The trap states on the SiO$_2$ substrate capture the electron–hole pairs generated by the photo power thereby reduce the photocurrent.[55] We checked the trap states in both devices by fitting the photocurrent ($I_{ph} = I_{illumination} - I_{dark}$) plotted as a function of P at $V_{ds} = 0$ V with the power–law equation $I_{ph} = aP^{\alpha}$, where a is a scaling constant and α an exponent,[30,56] as shown in Fig. 6(a) and (b) for device1 and device2 respectively. The value of α closer to 1 indicates a higher efficiency of photo-excited electron–hole pair generation and

also indicates fewer trap states at the junction ($\alpha = 1$ for ideal case). In our case α in device2 is about 0.87, which is higher than 0.69 in device1 indicating lower trap states in device2 with the h-BN substrate.

We also calculated the photo-responsivity (R) and external quantum efficiency (EQE). R is defined by$R = \dfrac{I_{ph}}{PS}$ where S is the junction area of the device. We show R as a function of P with 0 V$_{ds}$ and 0 V$_{bg}$ in Fig. 6(c). The observed increase of R as P decreases is in consistence with the articles published before.[30,57,58] R is about 3.0 A W^{-1} and 1.6 A W^{-1} with power density of 10 mW cm^{-2} for device2 and device1, respectively. The EQE is defined as the number of photo-generated carriers
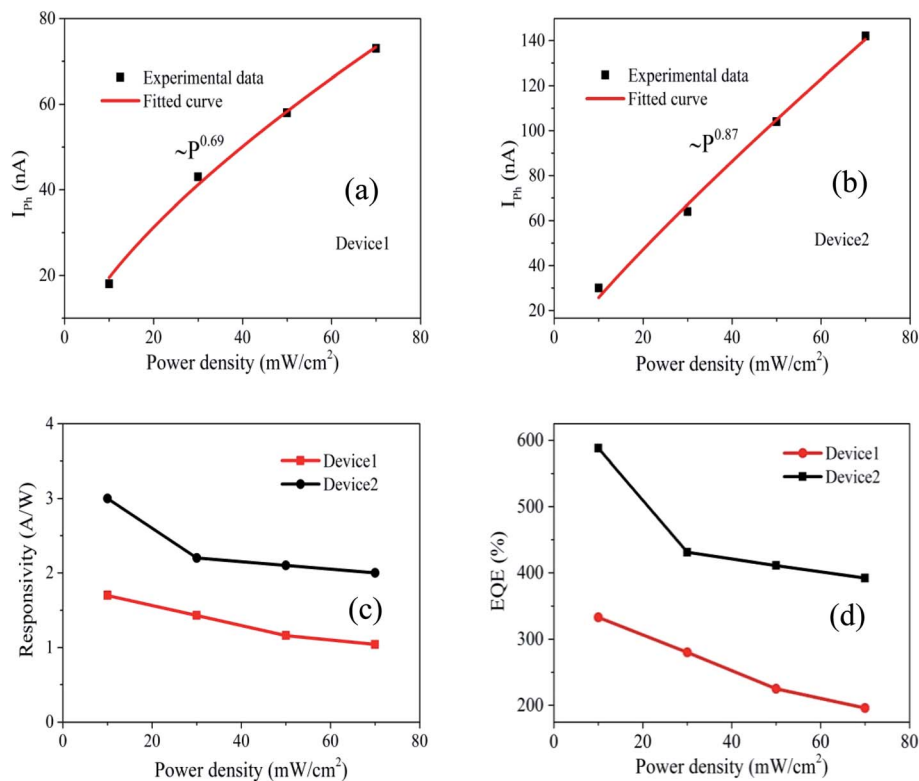
Fig. 6 (a) and (b) Self-driven photocurrent (I_{Ph}) vs. incident photo-power density on device1 and device2 respectively, where red curves show the power-law fitting. (c) and (d) Responsivity and EQE as a function of power density, respectively.

per incident photons per second and expressed as $\text{EQE} = \dfrac{Rhc}{e\lambda}$, where h is the Planck's constant, c the speed of light, and e the elementary charge. The value of EQE depends on the photo absorption and the accumulation of photo-generated carriers. Fig. 6(d) illustrates the values of EQE as a function of P at 0 V_{ds} and 0 V_{bg}. EQE is about 588% at 10 mW cm^{-2} for device2, which is about 2 times higher than that for the device1. These values we obtained in device2 are far better than the values reported before with the identical conditions in TMD hetero-structures.[28–30,58,59] The higher values of R and EQE in our device2 is mainly attributed to the use of h-BN substrate, which enhances the photo absorption and the photocurrent due to the lower trap states,[59,60] as well as the excellent photo response of WSe$_2$ (ref. 61–63) and WS$_2$ (ref. 24) as compared to other TMDs. In addition, a fast photo-carrier separation and the resulting short transit time due to the large built-in potential may contribute to a significant gain and the large EQE.[58,64,65]

Conclusion

We have investigated the electric and opto-electric properties of p-WSe$_2$/n-WS$_2$ vdW heterojunction diode on SiO$_2$ and h-BN substrates. The device on the h-BN substrate showed much enhanced diode characteristics. We have achieved more than an order-of-magnitude enhancement in the diode RR (>10^6) and better device stability with h-BN substrate over the SiO$_2$ substrate. Moreover, overall two-fold higher values were obtained in the photovoltaic characteristics on the h-BN substrate.

Particularly, the values of self-powered photo responsivity and EQE we have obtained are 3 A W^{-1} and 588% on the h-BN substrate at $P = 10$ mW cm^{-2} and $\lambda = 633$ nm. These values are superior to the values reported before at the identical conditions. The overall excellent results in device2 are mainly attributed to the use of inert, flat, and defect-free h-BN substrate, which reduces the carriers to be trapped in defect states. Moreover the heterostructure formed by highly photo-sensitive WS$_2$ and WSe$_2$ also plays a crucial role for the excellent photovoltaic outcome. To conclude, diode characteristics either electrical or opto-electrical can be significantly improved with the use of h-BN as a substrate and also with an appropriate selection of TMDs for the heterostructure.

Conflicts of interest

There are no conflicts to declare.

Acknowledgements

References

1 A. H. Castro Neto, *et al.*, The electronic properties of graphene, *Rev. Mod. Phys.*, 2009, **81**(1), 109–162.

2 T. Ando, The electronic properties of graphene and carbon nanotubes, *NPG Asia Mater.*, 2009, **1**(1), 17–21.

3 F. Bonaccorso, *et al.*, Graphene photonics and optoelectronics, *Nat. Photonics*, 2010, **4**(9), 611.

4 F. H. Koppens, D. E. Chang and F. J. Garcia de Abajo, Graphene plasmonics: a platform for strong light–matter interactions, *Nano Lett.*, 2011, **11**(8), 3370–3377.

5 N. Tombros, *et al.*, Electronic spin transport and spin precession in single graphene layers at room temperature, *Nature*, 2007, **448**(7153), 571–574.

6 P. Zomer, *et al.*, Long-distance spin transport in high-mobility graphene on hexagonal boron nitride, *Phys. Rev. B*, 2012, **86**(16), 161416.

7 P. R. Sharma, *et al.*, Magnetoresistance effect in a vertical spin valve fabricated with a dry-transferred CVD graphene and a resist-free process, *Mater. Res. Express*, 2020, **7**, 085603.

8 A. A. Green and M. C. Hersam, Emerging methods for producing monodisperse graphene dispersions, *J. Phys. Chem. Lett.*, 2010, **1**(2), 544–549.

9 D. C. Elias, *et al.*, Control of graphene's properties by reversible hydrogenation: evidence for graphane, *Science*, 2009, **323**(5914), 610–613.

10 K. Novoselov, Nobel lecture: Graphene: Materials in the flatland, *Rev. Mod. Phys.*, 2011, **83**(3), 837.

11 M. Kang, *et al.*, Universal mechanism of band-gap engineering in transition-metal dichalcogenides, *Nano Lett.*, 2017, **17**(3), 1610–1615.

12 Q. Wang, K. Kalantar-Zadeh, A. Kis, J. N. Coleman and M. S. Strano, *Nat. Nanotechnol.*, 2012, **7**, 699–712.

13 H. Tan, *et al.*, Ultrathin 2D photodetectors utilizing chemical vapor deposition grown WS_2 with graphene electrodes, *ACS Nano*, 2016, **10**(8), 7866–7873.

14 F. Koppens, *et al.*, Photodetectors based on graphene, other two-dimensional materials and hybrid systems, *Nat. Nanotechnol.*, 2014, **9**(10), 780–793.

15 Z. Sun, A. Martinez and F. Wang, Optical modulators with 2D layered materials, *Nat. Photonics*, 2016, **10**(4), 227–238.

16 J. A. Tatum and J. K. Guenter, Consumer electronics with optical communication interface, *US Pat.* 7,706,692, 2010.

17 B. Radisavljevic, M. B. Whitwick and A. Kis, Integrated circuits and logic operations based on single-layer MoS_2, *ACS Nano*, 2011, **5**(12), 9934–9938.

18 H. Fang, *et al.*, Degenerate n-doping of few-layer transition metal dichalcogenides by potassium, *Nano Lett.*, 2013, **13**(5), 1991–1995.

19 F. Dybała, *et al.*, Pressure coefficients for direct optical transitions in MoS_2, $MoSe_2$, WS_2, and WSe_2 crystals and semiconductor to metal transitions, *Sci. Rep.*, 2016, **6**, 26663.

20 J. Kopaczek, *et al.*, Direct optical transitions at K-and H-point of Brillouin zone in bulk MoS_2, $MoSe_2$, WS_2, and WSe_2, *J. Appl. Phys.*, 2016, **119**(23), 235705.

21 G. Rubio-Bollinger, *et al.*, Enhanced visibility of MoS_2, $MoSe_2$, WSe_2 and black-phosphorus: making optical identification of 2D semiconductors easier, *Electronics*, 2015, **4**(4), 847–856.

22 H. Yuan, *et al.*, Zeeman-type spin splitting controlled by an electric field, *Nat. Phys.*, 2013, **9**(9), 563–569.

23 D. Xiao, *et al.*, Coupled spin and valley physics in monolayers of MoS_2 and other group-VI dichalcogenides, *Phys. Rev. Lett.*, 2012, **108**(19), 196802.

24 N. Huo, *et al.*, Photoresponsive and gas sensing field-effect transistors based on multilayer WS_2 nanoflakes, *Sci. Rep.*, 2014, **4**, 5209.

25 A. Eftekhari, Tungsten dichalcogenides (WS_2, WSe_2, and WTe_2): materials chemistry and applications, *J. Mater. Chem. A*, 2017, **5**(35), 18299–18325.

26 H. Li, *et al.*, Mechanical exfoliation and characterization of single-and few-layer nanosheets of WSe_2, TaS_2, and $TaSe_2$, *Small*, 2013, **9**(11), 1974–1981.

27 H. Fang, *et al.*, High-performance single layered WSe_2 p-FETs with chemically doped contacts, *Nano Lett.*, 2012, **12**(7), 3788–3792.

28 N. Flöry, *et al.*, A $WSe_2/MoSe_2$ heterostructure photovoltaic device, *Appl. Phys. Lett.*, 2015, **107**(12), 123106.

29 M. M. Furchi, *et al.*, Photovoltaic effect in an electrically tunable van der Waals heterojunction, *Nano Lett.*, 2014, **14**(8), 4785–4791.

30 N. Huo, *et al.*, Tunable Polarity Behavior and Self-Driven Photoswitching in p-WSe_2/n-WS_2 Heterojunctions, *Small*, 2015, **11**(40), 5430–5438.

31 Y. Gong, *et al.*, Vertical and in-plane heterostructures from WS_2/MoS_2 monolayers, *Nat. Mater.*, 2014, **13**(12), 1135–1142.

32 R. Zhou, V. Ostwal and J. Appenzeller, Vertical *versus* lateral two-dimensional heterostructures: on the topic of atomically abrupt p/n-junctions, *Nano Lett.*, 2017, **17**(8), 4787–4792.

33 X. Duan, *et al.*, Lateral epitaxial growth of two-dimensional layered semiconductor heterojunctions, *Nat. Nanotechnol.*, 2014, **9**(12), 1024–1030.

34 L. Liao, *et al.*, Single-layer graphene on Al_2O_3/Si substrate: better contrast and higher performance of graphene transistors, *Nanotechnology*, 2009, **21**(1), 015705.

35 C. R. Dean, *et al.*, Boron nitride substrates for high-quality graphene electronics, *Nat. Nanotechnol.*, 2010, **5**(10), 722–726.

36 M. Ishigami, *et al.*, Atomic structure of graphene on SiO_2, *Nano Lett.*, 2007, **7**(6), 1643–1648.

37 R. Decker, *et al.*, Local electronic properties of graphene on a BN substrate *via* scanning tunneling microscopy, *Nano Lett.*, 2011, **11**(6), 2291–2295.

38 C. Lee, *et al.*, Comparison of trapped charges and hysteresis behavior in hBN encapsulated single MoS_2 flake based field effect transistors on SiO_2 and hBN substrates, *Nanotechnology*, 2018, **29**(33), 335202.

39 E. Wu, *et al.*, Dynamically controllable polarity modulation of $MoTe_2$ field-effect transistors through ultraviolet light and electrostatic activation, *Sci. Adv.*, 2019, **5**(5), eaav3430.

40 M. W. Iqbal, *et al.*, High-mobility and air-stable single-layer WS_2 field-effect transistors sandwiched between chemical vapor deposition-grown hexagonal BN films, *Sci. Rep.*, 2015, **5**, 10699.

41 W. Zhao, *et al.*, Lattice dynamics in mono-and few-layer sheets of WS_2 and WSe_2, *Nanoscale*, 2013, **5**(20), 9677–9683.

42 A. Berkdemir, *et al.*, Identification of individual and few layers of WS$_2$ using Raman Spectroscopy, *Sci. Rep.*, 2013, **3**(1), 1755.

43 X. Zhang, *et al.*, Defect-controlled nucleation and orientation of WSe$_2$ on hBN: a route to single-crystal epitaxial monolayers, *ACS Nano*, 2019, **13**(3), 3341–3352.

44 G.-H. Lee, *et al.*, Flexible and transparent MoS$_2$ field-effect transistors on hexagonal boron nitride-graphene heterostructures, *ACS Nano*, 2013, **7**(9), 7931–7936.

45 Y. Uchiyama, *et al.*, *Indirect bandgap of hBN-encapsulated monolayer MoS$_2$.* arXiv preprint arXiv:1903.06427, 2019.

46 C. Kim, *et al.*, Fermi level pinning at electrical metal contacts of monolayer molybdenum dichalcogenides, *ACS Nano*, 2017, **11**(2), 1588–1596.

47 A. Rai, *et al.*, Progress in contact, doping and mobility engineering of MoS$_2$: an atomically thin 2D semiconductor, *Crystals*, 2018, **8**(8), 316.

48 A. Allain and A. Kis, Electron and Hole Mobilities in Single-Layer WSe$_2$, *ACS Nano*, 2014, **8**(7), 7180–7185.

49 Y. Deng, *et al.*, Black phosphorus–monolayer MoS$_2$ van der Waals heterojunction p–n diode, *ACS Nano*, 2014, **8**(8), 8292–8299.

50 R. Cheng, *et al.*, Electroluminescence and photocurrent generation from atomically sharp WSe$_2$/MoS$_2$ heterojunction p–n diodes, *Nano Lett.*, 2014, **14**(10), 5590–5597.

51 A. M. Afzal, *et al.*, Tunneling-based rectification and photoresponsivity in black phosphorus/hexagonal boron nitride/rhenium diselenide van der Waals heterojunction diode, *Nanoscale*, 2020, **12**(5), 3455–3468.

52 C.-H. Lee, *et al.*, Atomically thin p–n junctions with van der Waals heterointerfaces, *Nat. Nanotechnol.*, 2014, **9**(9), 676.

53 H.-M. Li, *et al.*, Ultimate thin vertical p–n junction composed of two-dimensional layered molybdenum disulfide, *Nat. Commun.*, 2015, **6**(1), 1–9.

54 P. J. Jeon, *et al.*, Dipole-containing encapsulation on WSe$_2$/MoS$_2$ nanoflake pn diode with glass substrate toward an ideal performance. arXiv preprint arXiv:1412.7593, 2014.

55 M. Hafeez, *et al.*, Large-area bilayer ReS$_2$ film/multilayer ReS$_2$ flakes synthesized by chemical vapor deposition for high performance photodetectors, *Adv. Funct. Mater.*, 2016, **26**(25), 4551–4560.

56 M. Wasala, *et al.*, Effect of underlying boron nitride thickness on photocurrent response in molybdenum disulfide-boron nitride heterostructures, *J. Mater. Res.*, 2016, **31**(7), 893.

57 G. Konstantatos, *et al.*, Hybrid graphene–quantum dot phototransistors with ultrahigh gain, *Nat. Nanotechnol.*, 2012, **7**(6), 363–368.

58 H. Luo, *et al.*, High-Responsivity Photovoltaic Photodetectors Based on MoTe$_2$/MoSe$_2$ van der Waals Heterojunctions, *Crystals*, 2019, **9**(6), 315.

59 X. Wei, *et al.*, Photodetectors based on junctions of two-dimensional transition metal dichalcogenides, *Chin. Phys. B*, 2017, **26**(3), 038504.

60 G. Nazir, *et al.*, Comparison of electrical and photoelectrical properties of ReS$_2$ field-effect transistors on different dielectric substrates, *ACS Appl. Mater. Interfaces*, 2018, **10**(38), 32501–32509.

61 N. R. Pradhan, *et al.*, High photoresponsivity and short photoresponse times in few-layered WSe$_2$ transistors, *ACS Appl. Mater. Interfaces*, 2015, **7**(22), 12080–12088.

62 J. Lu, *et al.*, Atomic healing of defects in transition metal dichalcogenides, *Nano Lett.*, 2015, **15**(5), 3524–3532.

63 W. Zhang, *et al.*, Role of metal contacts in high-performance phototransistors based on WSe$_2$ monolayers, *ACS Nano*, 2014, **8**(8), 8653–8661.

64 N. Oliva, *et al.*, Van der Waals MoS$_2$/VO$_2$ heterostructure junction with tunable rectifier behavior and efficient photoresponse, *Sci. Rep.*, 2017, **7**(1), 14250.

65 M. Hussain, *et al.*, NIR self-powered photodetection and gate tunable rectification behavior in 2D GeSe/MoSe$_2$ heterojunction diode, *Sci. Rep.*, 2021, **11**(1), 3688.